J Mater Sci (2020) 55:8610–8629

Electronic materials

Growth mechanism and vibrational and optical properties of $SrMoO_4$: Tb^{3+}, Sm^{3+} particles: green–orange tunable color

D. F. Dos Santos[1], L. X. Lovisa[1,*], A. A. G. Santiago[1], M. Siu Li[2], E. Longo[3], M. R. D. Bomio[1], and F. V. Motta[1]

[1] LSQM – Laboratory of Chemical Synthesis of Materials – Department of Materials Engineering, Federal University of Rio Grande do Norte, P.O. Box 1524, Natal, RN 59078-900, Brazil
[2] IFSC, USP, Av. Trabalhador São Carlense, 400, São Carlos, SP CEP 13566-590, Brazil
[3] CDMF-LIEC, UFSCar, P.O. Box 676, São Carlos, SP 13565-905, Brazil

Received: 12 December 2019
Accepted: 30 March 2020
Published online: 10 April 2020

ABSTRACT

A $SrMoO_4$ series co-doped with Tb^{3+} and Sm^{3+} was successfully prepared by the sonochemical method. The particles were characterized by X-ray diffraction, Raman spectroscopy, field emission gun scanning electron microscopy, UV–Vis spectroscopy and photoluminescence. Changes in $SrMoO_4$: Tb^{3+}, Sm^{3+} morphologies were observed from an orderly growth of the particles. The mechanism of particle growth was proposed, indicating a hierarchical evolution of $SrMoO_4$: Tb^{3+}, Sm^{3+} morphologies. The changes in emissions were evaluated by the effect of the dopants and their concentrations. Emissions were observed in white, green and orange according to the chemical composition of the samples. The $SrMoO_4$ and $SrMoO_4$: 1% Sm samples showed excellent results for CRI (79%) and LE (> 310 lm/W_{opt}), thus indicating a material with potential for efficient white light emission.

Introduction

The use of rare-earth ions in luminescent materials has increased in recent years due to the great interest in studying optical and spectral properties [1, 2]. The energy transfer between doping elements in an inorganic host matrix has been studied for the luminescent behavior in the area of photonics and optoelectronics due to their technological application [3, 4].

Luminescence of a rare-earth ion from the use of a sensitizer (**S**) will be higher compared to direct activation of the activator (**A**) due to the energy transfer being favorable to the activator, and further improvements in intensity can be achieved by combining (**S**) and (**A**) [5, 6]. According to Pavani et al. [7], the choice of host material to be used must be

Address correspondence to E-mail: lauraengmat@hotmail.com

https://doi.org/10.1007/s10853-020-04623-5

made carefully to meet the appropriate requirements for the use of optical devices.

Scheelite structures have been successfully used as a host matrix of rare-earth ions due to their structural, chemical and optical properties [8]. These structures exhibit excellent thermal and chemical stability, as well as a high solubility of rare-earth dopants. This property group met excellent conditions for application of host materials [9–11]. The scheelite structure ($XMoO_4$, X = alkaline ions) has great potential in technological applications such as luminescent hosts, self-emitting materials, microwave applications and catalysts [12–15] due to their aforementioned properties.

$SrMoO_4$ exhibits excellent luminescence properties in the blue and green spectral regions, so it can be used as a kind of self-activated luminescent material [16]. Several types of research have been conducted with $SrMoO_4$ aiming at the production of white light from the combination of several doping ions. Shivakumara and Saraf [17] and Xu et al. [18] demonstrated the use of Eu^{3+} in the $SrMoO_4$ matrix, obtaining the red light from the matrix. Yang et al. [19] investigated the photoluminescent behavior of Eu^{3+}- and Tb^{3+}-doped $SrMoO_4$ separately. Niu et al. [20] achieved yellowish-white emission from Dy^{3+}-doped $SrMoO_4$, while red and green emission was obtained for Eu^{3+}- and Tb^{3+}-doped samples, respectively.

This study aims to synthesize, characterize and study the structural, vibrational, morphological, photocatalytic and photoluminescent properties of $SrMoO_4$ and $SrMoO_4$ series particles: 1% Tb, x% Sm (x = 1, 1.5, 2). An evolution mechanism of $SrMoO_4$ particle morphology is shown as a proposal for crystal growth. In addition, the photoluminescence processes and the possible expected energy transfers of the material are presented. The photocatalytic property of $SrMoO_4$: Tb^{3+}, Sm^{3+} was also evaluated in parallel to the study of photoluminescence. The effect of Tb^{3+} and Sm^{3+} doping on the crystalline lattice and the band structure of $SrMoO_4$ is highlighted.

Experimental procedure

Materials

Sodium molybdenum oxide dihydrate [$Na_2MoO_4 \cdot 2H_2O$, Alfa Aesar], strontium nitrate [$Sr(NO_3)_2$, Alfa Aesar], terbium oxide [Tb_4O_7, Aldrich], samarium(III) nitrate hexahydrate [$Sm(NO_3)_3 \cdot 6H_2O$, Aldrich], nitric acid [HNO_3, Synth], ammonium hydroxide [NH_4OH, Synth] and distilled water were used as reagents to prepare the $SrMoO_4$ and $SrMoO_4$: Tb^{3+}, Sm^{3+} particles.

Sonochemical synthesis of the $SrMoO_4$ and $SrMoO_4$: Tb^{3+}, Sm^{3+} particles

Two precursor solutions were prepared for the synthesis of the $SrMoO_4$, $SrMoO_4$: 1% Tb^{3+}, $SrMoO_4$: 1% Sm^{3+} and $SrMoO_4$: 1% Tb^{3+}, x% Sm^{3+} (x = 1, 1.5, 2) particles. Solution A corresponds to molybdenum with a (C_0) concentration of 0.201 mol/L. Solution B refers to strontium with a concentration (C_0) of 0.201 mol/L, with a molar ratio of 1:1. Solution B was added to solution A by dripping it under constant magnetic stirring. The dopants were then added one at a time. Tb^{3+} was added from a solution in HNO_3 with a concentration equal to 1.364×10^{-2} mol/L. The Sm^{3+} precursor because it is a nitrate [$Sm(NO_3)_3 \cdot 6H_2O$] is totally soluble in the reaction medium. Then, it was added directly to the solution in stoichiometrically calculated and weighed values. All precursors were stoichiometrically weighed. The pH of the final solution was adjusted to 8 from the addition of approximately 3 mL of NH_4OH, observing the formation of the precipitate. The pH value for all syntheses performed was kept constant. The final solution was exposed to intense ultrasonic radiation with 65% amplitude in the continuous mode for 20 min. The precipitates were washed and centrifuged three times in distilled water and then kept in the oven at a temperature of 80 °C for 24 h for drying. An ultrasonic processor (S-450, Branson Ultrasonics Sonifier) with a power of 400 Watts and a frequency of 25 kHz was used. This processor enables programming the amplitude of the waves emitted by the ultrasonic tip at a pre-selected level, so that the irradiation of the waves in the solution can be controlled.

Characterizations

The $SrMoO_4$ and $SrMoO_4$: Tb^{3+}, Sm^{3+} particles were structurally characterized by XRD using a Shimadzu XRD 7000 instrument with Cu-Kα radiation (λ = 1.5406 Å) in the 2θ range from 10° to 80° at a scanning rate of 0.02 s^{-1}. Raman spectroscopy

spectra were measured by FT-Raman Bruker-RFS 100 using an Nd:YAG laser operating at 1064 nm with nominal power of 55 mW as the excitation source. The morphologies were investigated using a field emission gun scanning electron microscope (FE-SEM; Carl Zeiss, Supra 35-VP Model, Germany) operated at 6 kV. The UV–Vis diffuse reflectance spectrum was measured at room temperature using a Shimadzu UV-2600 spectrophotometer. The photoluminescence (PL) spectra were acquired with an Ash Monospec 27 monochromator (Thermal Jarrel, USA) and an R4446 photomultiplier (Hamamatsu Photonics, USA). The 325-nm beam of a krypton ion laser (Coherent Innova 90 K) was used as the excitation source with an output of approximately 13.3 mW. All measurements were taken at room temperature.

The photocatalytic properties of the powders combined as a catalyst agent were estimated by the degradation of the methyl orange (MO) with a molecular formula [$C_{14}H_{14}N_3NaO_3S$] (99.5% purity, Mallinckrodt), illuminated by UV lamps in aqueous solution. First, 50 mL of the MO solution (1×10^{-5} mol L^{-1} concentration) was mixed with 0.05 g of the material and 0.05 mL oxygen peroxide to increase degradation to be tested in a quartz beaker. This mixture was kept under stirring at a controlled temperature (25 °C) and lit by six UVC lamps (15 W TUV Philips, with a maximum intensity of 254 nm = 4.9 eV). The sample was kept under stirring for 30 min with the lights off to disregard possible adsorption events. An aliquot of the samples was taken at each 5-minute time interval and centrifuged at 9000 rpm for 5 min to remove the suspended particles. Finally, the variations in the maximum absorption band of each aliquot were measured by UV–Vis absorbance with spectral measurements using a Shimadzu UV-2600 spectrophotometer with a wavelength in the range of 400 to 800 nm.

Results

X-ray diffraction

Figure 1-I represents the XRD patterns of the $SrMoO_4$, $SrMoO_4$: 1% Tb^{3+}, $SrMoO_4$: 1% Sm^{3+} and $SrMoO_4$: 1% Tb^{3+}, x% Sm^{3+} (x = 1, 1.5 and 2) samples. All peaks presented in the diffractograms are properly indexed with scheelite-type tetragonal structure with space group *I41/a* in agreement with the respective "Joint Committee on Powder Diffraction Standards" (JCPDS) card no. 850586. No peak was found for the secondary phases. $SrMoO_4$ was successfully synthesized by the sonochemical method without further heat treatment. Figure 1-II shows a displacement of the main peak (112) located at 27.82° when dopants (Tb^{3+}, Sm^{3+}) are introduced into the $SrMoO_4$ matrix. This displacement does not occur regularly with increasing doping concentration. This behavior can be attributed to the distortions in the $SrMoO_4$ structure due to the interactions generated by the effect of electron density caused in the doping process [6]. An excess of positive charges occurs when introducing dopants into the $SrMoO_4$ structure. Thus, Sr^{2+} vacancy defects arise to counteract the charges. The difference in Sr^{2+} electron density compared to Tb^{3+} and Sm^{3+} causes structural distortions in the $SrMoO_4$ lattice. These changes occur due to the inequality in the electronic densities between the lattice forming clusters and the doping clusters. The doping process promotes the emergence of Sr^{2+} vacancy sites which modify the position of the valence band energy levels with the simultaneous insertion of the Tb^{3+} and Sm^{3+} cation orbitals into the conduction band [6, 21, 22]. Figure 1-III illustrates the $SrMoO_4$ unit cell in a tetragonal crystalline system and space group *I41/a*. The ionic radii of Sr^{2+} (CN = 8), Mo^{6+} (CN = 4), Tb^{3+} (CN = 8) and Sm^{3+} (CN = 8) is 1.26, 0.41, 1.04 and 1.08 Å, respectively [23]. Thus, $Sr^{2+} \rightarrow Tb^{3+}/Sm^{3+}$ substitution occurs easily due to the proximity of the ionic radii. The unit cell of $SrMoO_4$ is formed by two different clusters, where Mo^{6+} cations are found in the unit cell of the material being coordinated by four O^{2-} anions in tetrahedral coordination [MoO_4], while Sr^{2+} cations are surrounded by eight O^{2-} anions in dodecahedral coordination [SrO_8] [24]. Chen et al. [25] described the primitive unit cell of this structure with two units of $SrMoO_4$, each with an inversion center. The authors also mentioned that Sr and Mo sites present S_4 point symmetry. In the $SrMoO_4$ crystalline structure, Sr–O bonds are characterized by a covalent/ionic character, while Mo–O bonds have a covalent nature across clusters [MoO_4]. Changes in lattice parameters generated by distortions in the crystalline lattice cause the change in bond length and bond electron energy levels. As a result, the charges and energy in nanostructures become densified and localized [26, 27].

Structure refinement using the Rietveld method was performed to confirm the tetragonal phase of

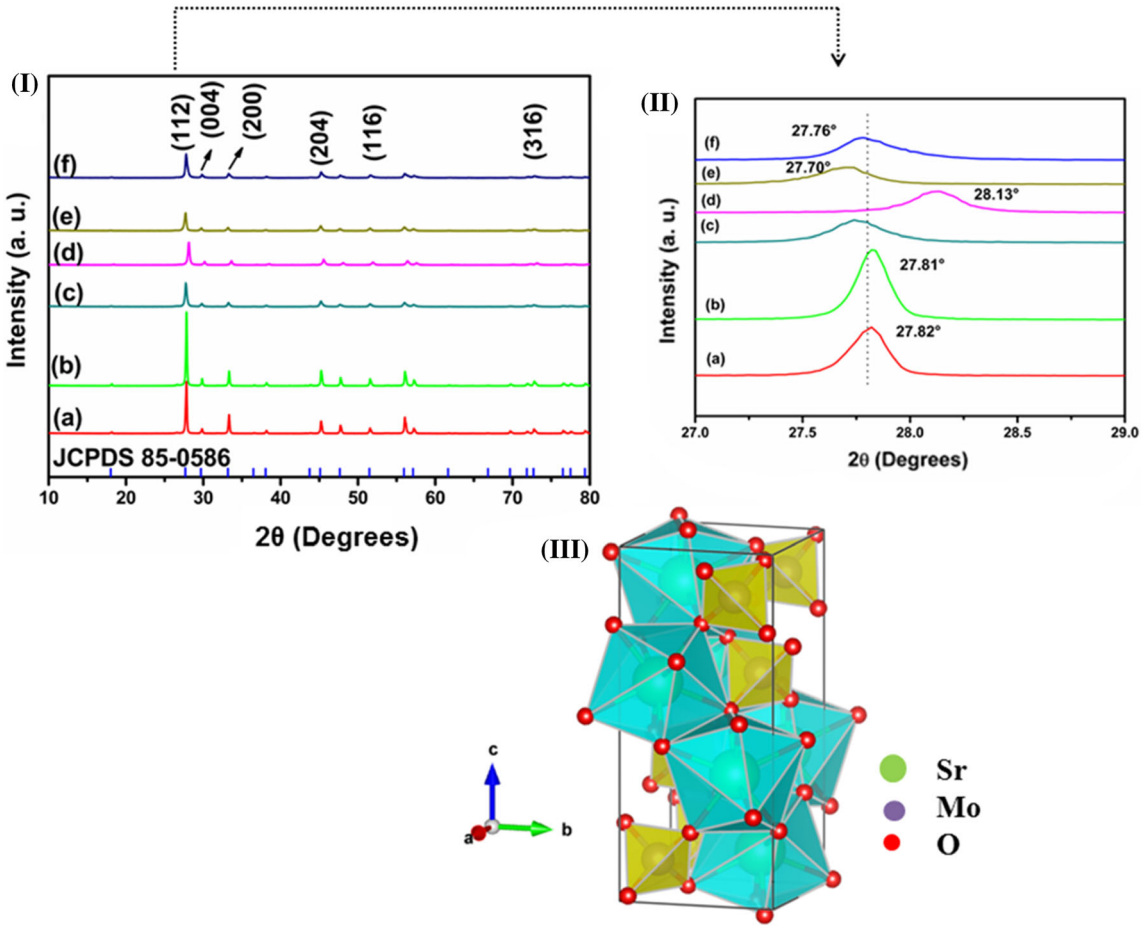

Figure 1 **I** XRD patterns of samples (*a*) $SrMoO_4$, (*b*) $SrMoO_4$: 1% Sm^{3+}, (*c*) $SrMoO_4$: 1% Tb^{3+}, (*d*) $SrMoO_4$: 1% Tb^{3+}, 1% Sm^{3+}, (*e*) $SrMoO_4$: 1% Tb^{3+}, 1.5% Sm^{3+}, (*f*) $SrMoO_4$: 1% Tb^{3+}, 2% Sm^{3+}; **II** peak displacement (112); and **III** representation of $SrMoO_4$ unit cell.

$SrMoO_4$ particles utilizing the General Structure Analysis System (GSAS) with an EXPGUI graphic interface [28]. Figure 2 represents the refinement graphs with good approximation between the experimental data and the data calculated by the Calc-Obs line. The Rietveld refined structural parameters are shown in Table S1 of the supplementary information.

Small alterations in lattice parameters were observed between samples due to the different doping performed, and a variation in crystallite size and cluster distortions are observed as a result. The cell volume tends to decrease with an increase in dopants due to Tb^{3+}/Sm^{3+} ionic radii becoming smaller than Sr^{2+} ionic radii. The crystallite size of the samples also decreased with doping. This behavior can be explained by the fact that the increase in the percentage of Tb^{3+}/Sm^{3+} cations was accompanied by an increase in the number of defects in the $SrMoO_4$ crystalline lattice, which increased the lattice tension. This behavior is similar to Vegard's law for solid two-component metallic solutions, which predicts that the unit cell dimensions of the solid solution vary linearly with the concentration of the solute component [29, 30].

Raman spectroscopy

The scheelite structure has molecular ion units $[XO_4]^{2-}$, (X = Mo, W), with strong covalent bonds of (X–O) and has a weak coupling with metallic cation (M^{2+}). The group theory calculation has 26 different vibrations for MXO_4 with zero wavevector crystals $(\vec{k} = 0)$ [31–33], as indicated in Eq. (2):

$$\Gamma = 3A_g + 5A_u + 5B_g + 3B_u + 5E_g + 5E_u \quad (2)$$

where the vibrations A_g, B_g and E_g are active modes in Raman and B is non-degenerate, while mode E is doubly degenerate. The indices "g" and "u" indicate

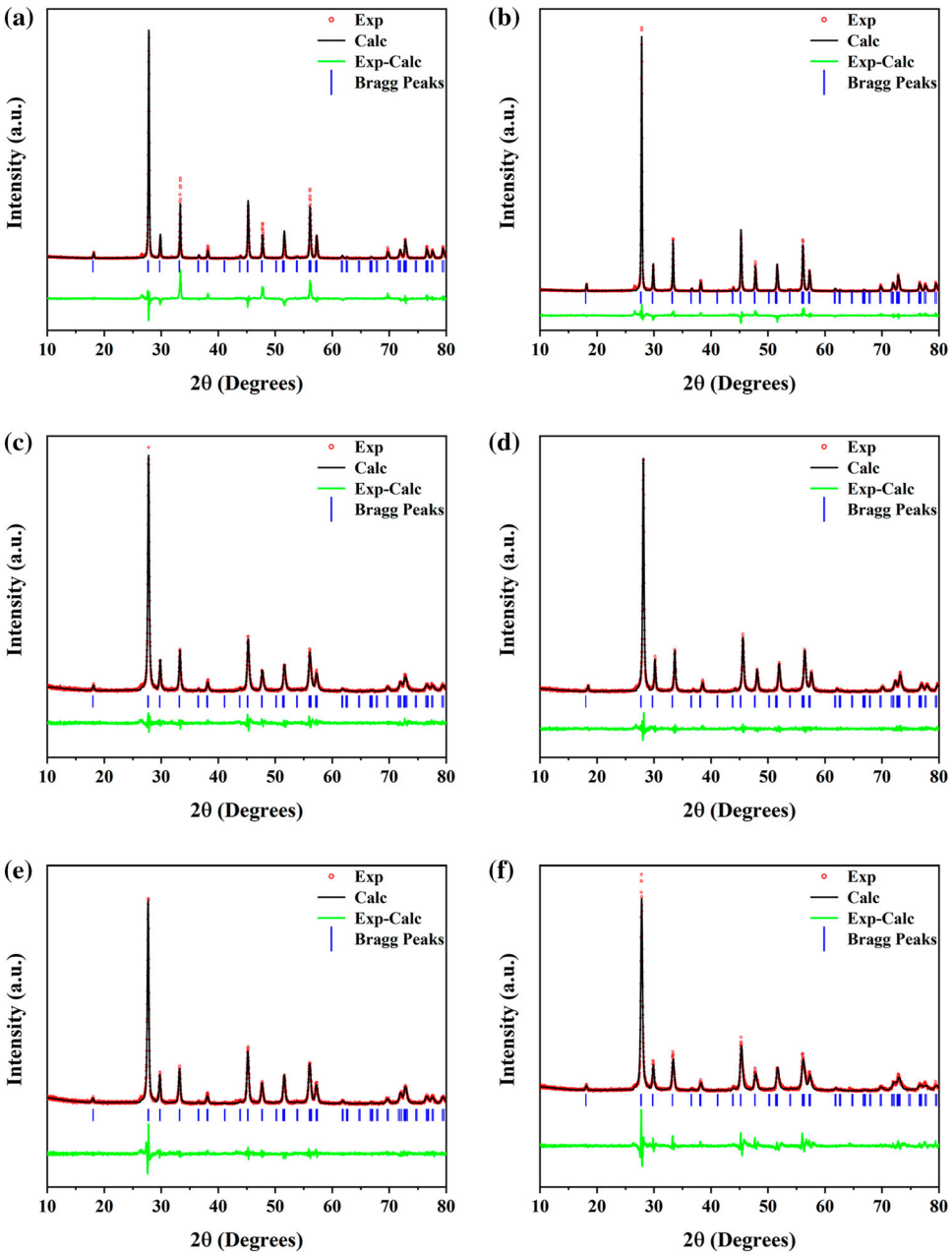

Figure 2 Observed, calculated and the difference in XRD patterns of $SrMoO_4$: Tb^{3+}, Sm^{3+} particles **a** $SrMoO_4$, **b** $SrMoO_4$: 1% Sm^{3+}, **c** $SrMoO_4$: 1% Tb^{3+}, **d** $SrMoO_4$: 1% Tb^{3+}, 1% Sm^{3+}, **e** $SrMoO_4$: 1% Tb^{3+}, 1.5% Sm^{3+}, **f** $SrMoO_4$: 1% Tb^{3+}, 2% Sm^{3+}.

the inverse parity in centrosymmetric crystals. The A_u and E_u modes correspond to the zero frequency of the acoustic modes, while the others are optical modes. In addition, modes A_g, B_g and E_g arise from the same motion as $SrMoO_4$ crystal. Therefore, 13 active zone-center Raman modes are expected for $SrMoO_4$, as shown in (3) [34, 35]:

$$\Gamma = 3A_g + 5B_g + 5E_g \quad (3)$$

Raman vibrational modes can be classified into two groups: external mode and internal mode. The first is related to the movement of M^{2+} cations in relation to the tetrahedral rigid units $[MoO_4]^{2-}$. The second is associated with vibrations within tetrahedral units $[MoO_4]^{2-}$ and is considered the steady state of the center of mass. The Raman spectra of the $SrMoO_4$ and $SrMoO_4$: Tb^{3+}, Sm^{3+} particles are shown in Fig. 3, and active modes in Raman are shown in Table S2 of the supplementary information.

The vibrations detected in the range between 100 and 1000 cm^{-1} are recorded. The $[MoO_4]^{2-}$ tetrahedra have symmetry T_d [36] and are composed of four internal modes [υ_1 (A1), υ_2 (E1), υ_3 (F2) and υ_4 (F2)], a

free rotation mode [$\upsilon_{f.r.}$ (F1)] and a translation mode (F2) [37].

The Raman peak at 885.51 cm^{-1} was assigned to the symmetric stretching vibration mode υ_1(Ag) of the $[MoO_4]^{2-}$ group in the $SrMoO_4$ crystal. The peaks at 842.0 and 793.0 cm^{-1} corresponded to the anti-symmetric stretching υ_3(Bg) and υ_3(Eg) vibration modes, respectively. The peaks at 365.0 and 325 cm^{-1} corresponded to the anti-symmetric and symmetric υ_4(Bg) and υ_2(Ag) bending modes, respectively.

As observed in Fig. 3, nine Raman-active vibrations were detected. According to Ling et al. [38], the strong and intense active modes in Raman suggest a strong interaction between ions, which appear from the elongation and flexural vibrations of the shorter metal–oxygen (Sr–O) bonds within the anionic groups. Raman spectrum is a powerful technique for assessing information about the level of short-range structural order–disorder in materials. The values in Table S2 show the variation in the vibration band positions. This behavior may be associated with the presence of defects, the interaction force between clusters, as well as the level of structural order–disorder in the lattice.

Field emission gun scanning electron microscopy (FE-SEM)

Figure 4 shows the FE-SEM images of $SrMoO_4$ and $SrMoO_4$: Tb^{3+}, Sm^{3+} particles. From the images in Fig. 4a–e, it can be seen that the $SrMoO_4$ and $SrMoO_4$: 1% Tb^{3+} samples have different morphology types in their particles. The particles have a rice shape (Fig. 4a, while others have a flower shape (Fig. 4b, e) or star shape (Fig. 4c, d). $SrMoO_4$: 1% Tb^{3+}; $SrMoO_4$: 1% Tb^{3+}, 1% Sm^{3+}; $SrMoO_4$: 1% Tb^{3+}, 1.5% Sm^{3+}; and $SrMoO_4$: 1% Tb^{3+}, 2% Sm^{3+} samples predominantly show rice-like morphology. Figure 4b shows the individual morphology of a flower-shaped particle set composed of petals of varying sizes. It is observed that the average particle size of $SrMoO_4$ and $SrMoO_4$: 1% Sm^{3+} is much larger than that found for the other samples. This information may be associated with the effect of Tb^{3+} as a growth retardant agent of the particles present in other samples. According to Table S1 of the supplementary information, the $SrMoO_4$ and $SrMoO_4$: 1% Sm^{3+} samples presented a much larger crystallite size than the other samples. This feature is indicated by the narrower appearance of the X-ray diffraction peaks, as shown in Fig. 1b.

Figure 5 is a schematic illustrating the growth steps of $SrMoO_4$ particles obtained by the sonochemical method. There are initially two precursor solutions (Sr^{2+} and MoO_4^{2-}). Then, the Sr^{2+} solution is added, and the molybdenum solution is added. This phase is characterized by the nucleation phase, with the formation of numerous $SrMoO_4$ nuclei. In the next step, it is observed that these nuclei begin to organize in a growth phase through the self-assembly process [39], wherein it is possible to observe the presence of rice-shaped microcrystals and the increase in particle size is favored by decreased surface energy. There is a progressive growth of $SrMoO_4$ microcrystals toward the emergence of new tips in the rice structures with the development of morphologies, thus producing

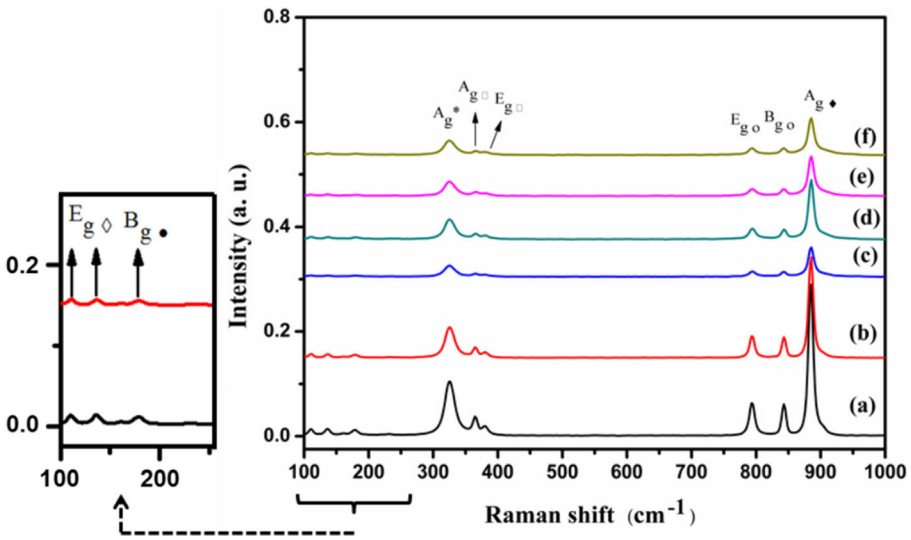

Figure 3 Raman spectra of $SrMoO_4$: Tb^{3+}, Sm^{3+} particles.

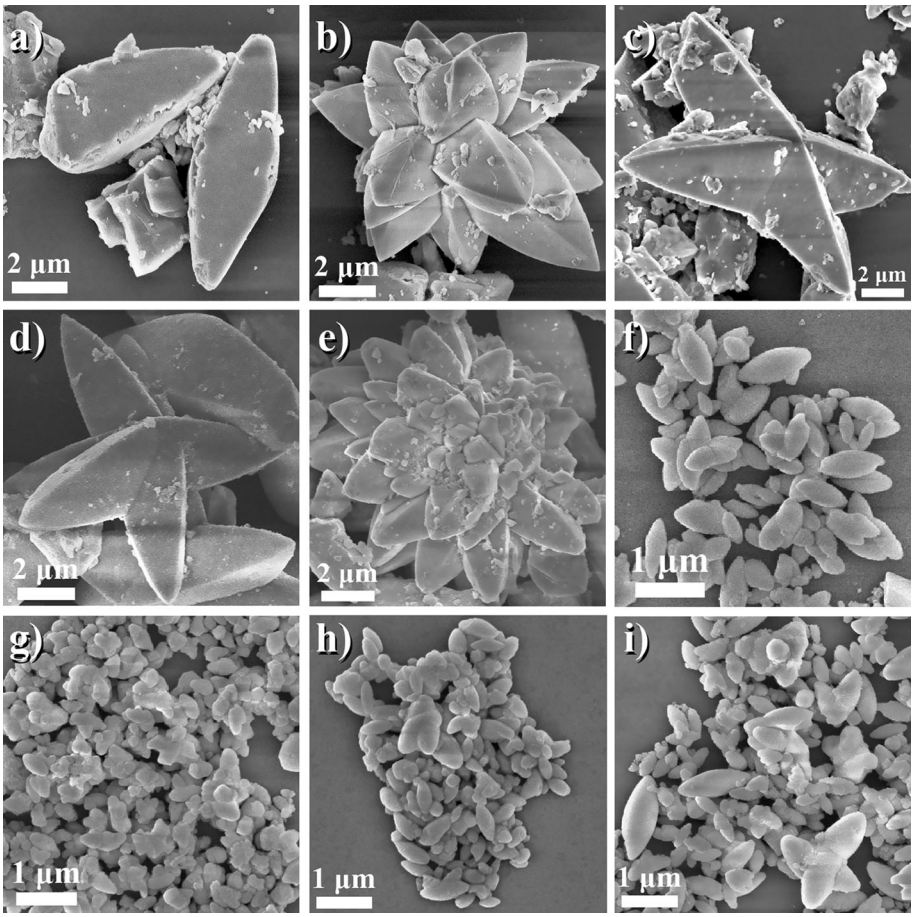

Figure 4 FE-SEM images of $SrMoO_4$ (**a**–**c**); $SrMoO_4$: 1% Sm^{3+} (**d**–**e**); $SrMoO_4$: 1% Tb^{3+} (**f**); $SrMoO_4$: 1% Tb^{3+}, 1% Sm^{3+} (**g**); $SrMoO_4$: 1% Tb^{3+}, 1.5% Sm^{3+} (**h**); and $SrMoO_4$: 1% Tb^{3+}, 2% Sm^{3+} (**i**).

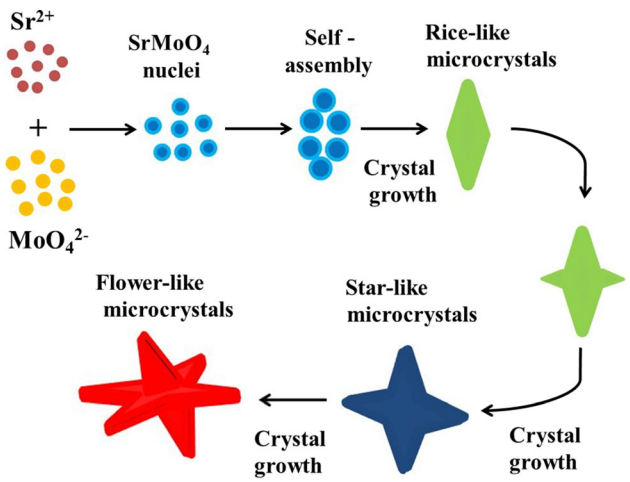

Figure 5 Scheme representative of the hierarchical evolution of $SrMoO_4$: Tb^{3+}, Sm^{3+} morphologies.

new particles with star shapes. New points in the structure then appear as the growth evolution proceeds, such that new flower-like shapes can be obtained. Cavalcante et al. [40] were able to produce $SrWO_4$ with various morphologies by the hot ion injection technique, for which they affirmed a directionality in particle growth found by XRD and TEM analyses.

The influence of the reaction medium pH significantly interferes with the particle morphology of $SrMoO_4$ [41]. Jiang el at. [42] evaluated the changes caused by $SrMoO_4$ particle shapes under pH as well as other conditions. They found that the morphology predominance was between "flower" and "rice" at pH levels between 6 and 11, while the particles had a tendency to wire formation for the acidic medium (pH = 4). According to Li and Zhang [43], the equilibrium between the different states of molybdate ions can be achieved by controlling the pH. Moreover, there is a predominance of MoO_4^{2-} ions under $Mo_7O_{24}^{6-}$ ions for pH higher than 6, which guarantees the necessary condition for the formation of small $SrMoO_4$ crystalline nuclei and subsequent growth. The MoO_4^{2-} concentration is low when the pH is below 6 and can be released in the presence of $Mo_7O_{24}^{6-}$. Free MoO_4^{2-} ions combine with Sr^{2+} cations to form $SrMoO_4$. According to the Gibbs–

Thomson law, large particles grow at the expense of smaller ones due to the difference in solubility. These smaller $SrMoO_4$ particles dissolve and grow along a preferential orientation assisted by the sonochemical process. According to the oriented attachment mechanism proposed by Penn and Banfield et al. [44, 45], larger particles are developed from small primary particles through an oriented fixation process in which the nanoparticles are self-assembled, sharing a common crystallographic orientation. Equation (4) models the effect of pH on molybdenum ion concentrations for $SrMoO_4$ formation.

$$Mo_7O_{24}^{6-} \leftrightarrows MoO4^{2-} + Sr^{2+} \rightarrow SrMoO_4 \quad (4)$$

The particle distribution is shown in Fig. S1 of the supplementary information The particle length for this analysis as indicated by the figure in the histograms was taken as the basis of measurement. It is observed that the average particle size is greatly influenced by the presence of Tb^{3+} in the $SrMoO_4$ structure. Pires et al. [46] observed a reduction in Eu^{3+}-doped Gd_2O_3 particle size and correlated this behavior with the presence of Eu^{3+} on the surface of Gd_2O_3 particles causing inhibition of crystal growth. Zhao and Tan [47] demonstrated that the size and morphology of $NaYF_4$ could be controlled simultaneously by adjusting the dopant Ce^{3+} concentration, verifying a decrease in particle size associated with increased concentration of Ce^{3+}. The $SrMoO_4$ and $SrMoO_4$: 1% Sm^{3+} samples have much larger particle sizes than those found for the other samples. As seen in FE-SEM Fig. 4f–i, a decrease in $SrMoO_4$ particle growth occurs by introducing Tb^{3+} as a dopant, signaled by a reduction in the mean particle value (x_c). About 45% of $SrMoO_4$ particles are between 7 and 9 μm in size, while 43% of $SrMoO_4$: 1% Sm^{3+} samples are around 9 to 11 μm. For the $SrMoO_4$: 1% Tb; $SrMoO_4$: 1% Tb, 1% Sm; $SrMoO_4$: 1% Tb^{3+}, 1.5% Sm^{3+}; and $SrMoO_4$: 1% Tb^{3+}, 2% Sm^{3+} samples, x_c values are associated with the respective quantities: 680 nm, 334 nm, 450 nm and 518 nm. The fitting curve used in the particle size distribution profiles is lognormal, with x_c as the mean particle size value for each sample.

According to the energy-dispersive X-ray spectroscopy (EDS) in Fig. 6, it appears that the $SrMoO_4$: 1% Tb^{3+}, 1% Sm^{3+} sample showed good homogeneity in their chemical composition as presented by the elemental mapping result.

UV–Vis

The UV–Vis absorption properties of the $SrMoO_4$: Tb^{3+}, Sm^{3+} samples are shown in Fig. 7. From the absorption spectra, it is clearly observed that the absorption of the material is mainly concentrated in the UV region. The absorption band is located between 200 and 400 nm and is attributed to the charge transfer of oxygen electrons (2*p*) moving to molybdenum, the central atom of the cluster $[MoO_4]^{2-}$ [31]. Low absorption of around 10% and a high reflectance close to 90% were found in the region between 400 and 800 nm. It is also observed that the presence of Tb^{3+} in the samples promotes an increase in its absorption band creaking, showing a shift toward the blue region. The Sm^{3+} ion exhibits an excitation range situated at 402 nm due to its energy levels located near this region [48]. The transition in the spectrum originates from the ground state $^6H_{5/2}$ to excited state $^4F_{7/2}$ of the Sm^{3+} configuration $^4f_5$. The optical absorption behavior can be influenced by crystallite size, structure tension and particle shape. The lattice strain leads to surface or interfaces trapping and localization of charges on the surface and influences the band gap values [27].

Figure 8 represents the diffuse reflectance spectra transformed into absorption spectra by the Kubelka–Munk method. The Kubelka–Munk Eq. (5) is described as follows:

$$\alpha = \frac{(1-R)^2}{2R} \quad (5)$$

where α is the absorption coefficient and R is the reflectivity. It is possible to estimate the gap band interval between the powdery diffuse reflection spectra from this relationship [49–51]. It is then possible to determine the energy gap from the Tauc ratio (6):

$$\alpha \propto \left(hv - E_g\right)^n \quad (6)$$

where E_g is the energy gap, hv is photon energy, and n is an index that assumes different values according to the nature of the electronic transition responsible for reflection (n = ½ for direct allowed transitions, n = 2 for indirect allowed transitions, n = 3/2 for direct prohibited transitions and n = 3 for indirect prohibited transitions [52, 53].

The transitions of scheelite-like tetragonal structure molybdates exhibit direct permitted transitions (n = ½) [8]. The direct-type transition is verified

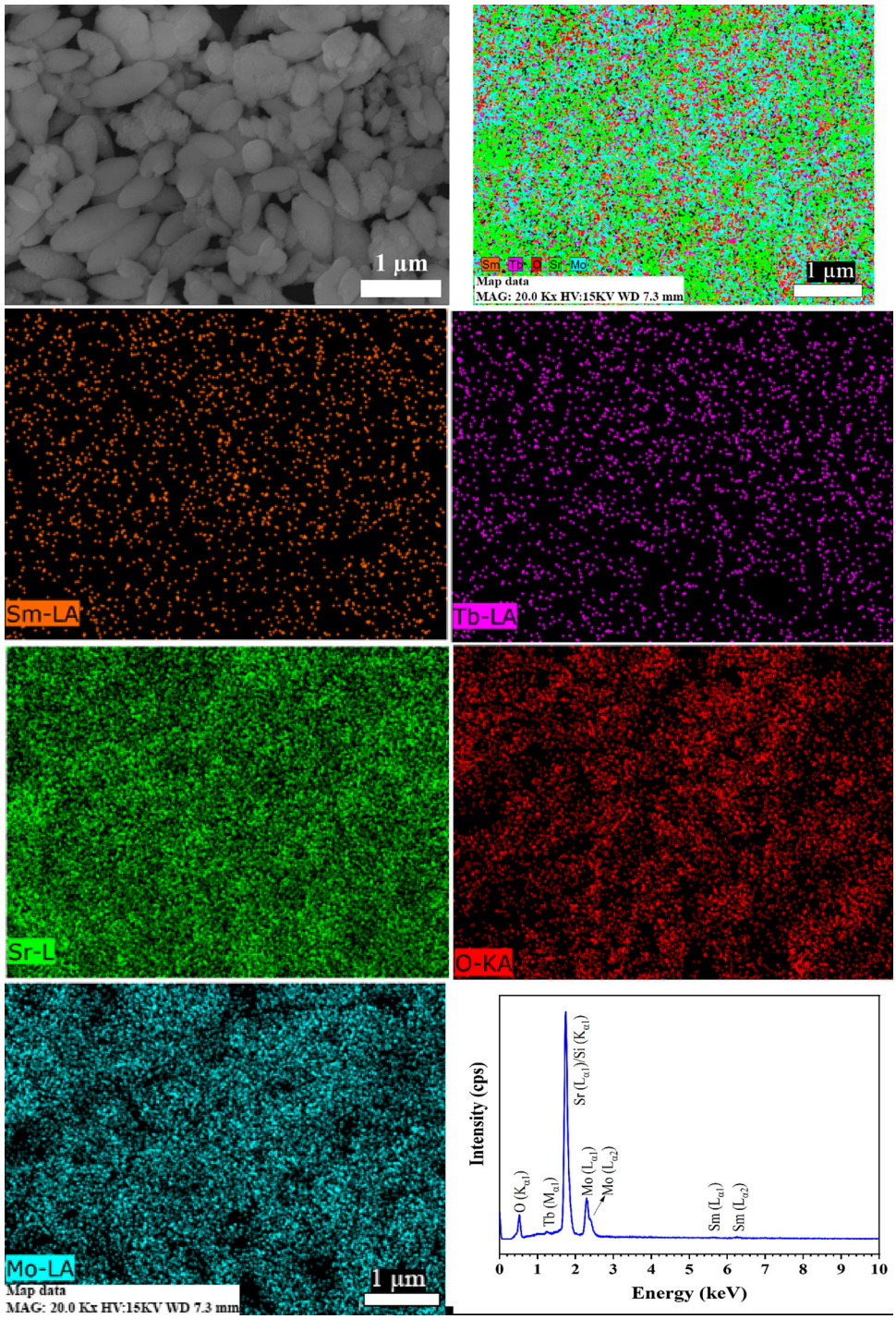

Figure 6 EDS spectrum and elemental mapping of $SrMoO_4$: 1% Tb^{3+}, 1% Sm^{3+}.

when the electronic transition occurs between the bottom of the conduction band and the top of the valence band at the same point of the Brillouin zone [54].

Figure 8 shows the graphs plotted between (αhv) on the ordinate axis vs hv on the abscissa axis. The E_g value is determined through extrapolation in the linear region of the curve for condition (αh) = 0.

The energy gap values found for $SrMoO_4$: Tb^{3+}, Sm^{3+} particles are in agreement with the studies reported in the literature, as indicated in Table S3 of the supplementary information. According to Zhu

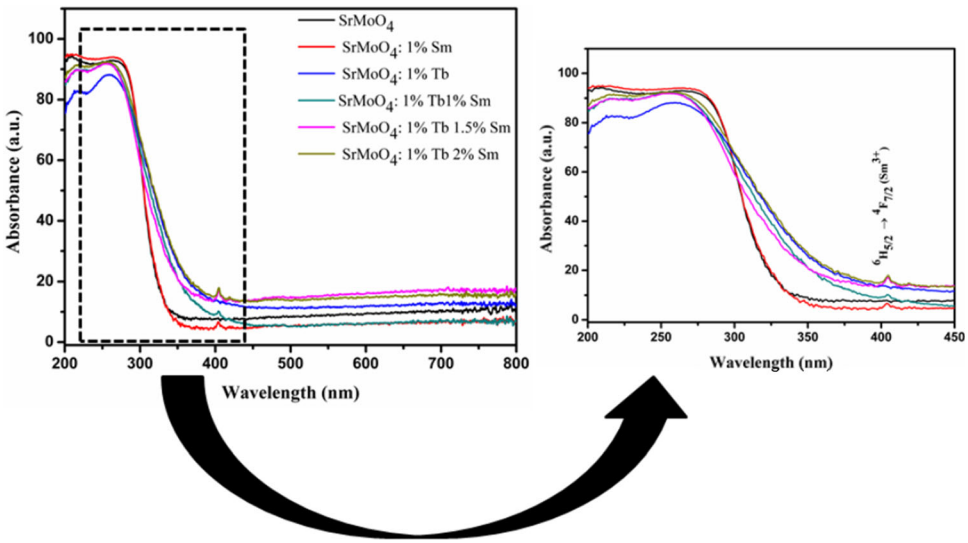

Figure 7 Optical absorption spectra of $SrMoO_4$: Tb^{3+}, Sm^{3+} samples.

et al. [55], the correlation of the decrease in energy gap value is associated with cluster distortions [MoO_4]. More precisely, this type of distortion promotes redistribution of the energy level within the gap and consequently leads to the formation of intermediate energy levels within the gap, which is basically composed of oxygen states 2*p* (above the valence band) and molybdenum 4*d* (near the driving band) [56]. According to Paradelas [57], the atoms that are located on the surface have unsatisfied valences and allow surface reconstruction as a way to reduce their surface energy, which in turn causes changes in the band structure from the emergence of energy levels within the forbidden region [58]. The authors [57] find it consistent that the particle size of the material interferes with the energy value of the gap, as well as the number of defects present in the structure and changes in the recombination rate of the electron–hole pair (e′–h·). These changes in material configurations translate into different results in the photocatalytic and photoluminescent properties of materials.

The energy gap values found for $SrMoO_4$: Tb^{3+}, Sm^{3+} particles are in agreement with the studies reported in the literature, as indicated in Table S3. Molybdenum atoms generally have an ideal position in the center of the tetrahedron, forming tetrahedral [MoO_4] clusters. However, the synthesis conditions of $SrMoO_4$ particles and the $Sr^{2+} \rightarrow Tb^{3+}/Sm^{3+}$ cation replacement process cause various distortions or the simultaneous presence of order–disorder in the lattice. These effects cause small displacements of Mo atoms in the center of symmetry of the tetrahedral clusters [MoO_4] [59]. The concentration of Tb^{3+}/Sm^{3+} ions is attributed to increased local lattice distortions and intermediate energy levels within the bandwidth range and local electronic density changes [22].

Photocatalytic properties

The photocatalytic activity of $SrMoO_4$: Tb^{3+}, Sm^{3+} particles was verified according to the concentration of methyl orange under UV irradiation for 45 min. H_2O_2 was used to increase the degradation rate. Figure 9 shows the variation of methyl orange dye concentration versus analysis time. Dye curves and dye with the peroxide curves were plotted for comparison. From the results shown in Fig. 9, it appears that the $SrMoO_4$ and $SrMoO_4$: 1% Sm^{3+} samples obtained the best results. The presence of Tb^{3+} represented a decrease in the photocatalytic activity of $SrMoO_4$. This can be related to the increase in the recombination rate of the hole + electron pair, which is translated by a smaller amount of free radicals, being the species responsible for the dye degradation [60].

The photoelectrons are excited from the valence band to the conduction band due to the narrowband aperture under visible-light irradiation, while the holes remain in the conduction band. Electrons and holes can effectively degrade methyl orange, accompanied by photosensitization. The electrons generated by the photo in the photosensitization process are immediately injected into the $SrMoO_4$ conduction band and react with the electron acceptors to produce

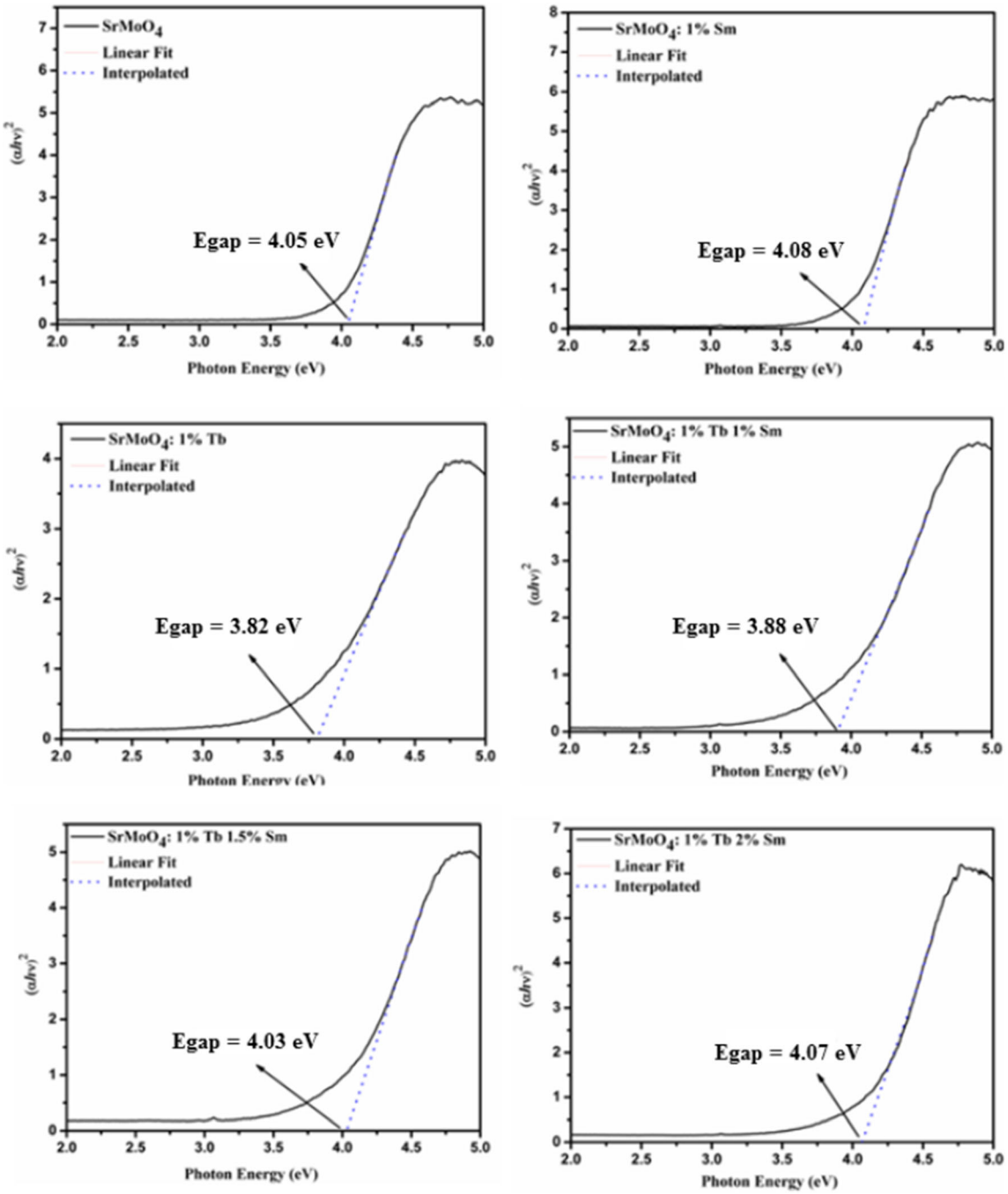

Figure 8 Energy gap of $SrMoO_4$: Tb^{3+}, Sm^{3+} samples.

the $O^{\cdot 2-}$ anion radical. The proposed mechanism of photocatalytic degradation of methyl orange can be assumed as [61]:

$$SrMoO_4 + hv \rightarrow SrMoO_4 + e^- + h^+ \quad (7)$$

$$h+ + H_2O \rightarrow OH^{\cdot} \quad (8)$$

$$e- + O_2^{\cdot} + \text{methyl orange} \rightarrow \text{degradation products} \quad (9)$$

It is well known that the energy band structure is a very important factor for the photocatalyst. It is also very important for the good performing photocatalyst to provide energetic electrons through an appropriate band interval, efficient photogenerated

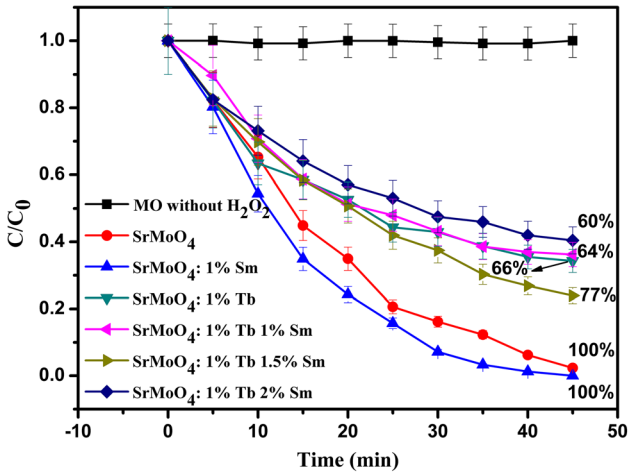

Figure 9 Normalized absorbance versus time for the photocatalytic discoloration of methyl orange.

charge separation and migration, and also strong inhibition of the photocorrosion process [62].

H_2O_2 is efficient for electron trapping by preventing the recombination of the electron + hole pair due to the photolysis of H_2O_2 to produce OH radicals, evidencing the increase in OH and O_2^- radicals on the catalyst surface.

$$H_2O_2 + HO^{\cdot} \rightarrow HO_2^{\cdot} + H_2O \quad (10)$$

$$H_2O_2 + e^- \rightarrow HO^{\cdot} + HO^- \quad (11)$$

$$H_2O_2 + O_2^{-\cdot} \rightarrow HO^{\cdot} + HO^- + O_2 \quad (12)$$

$$H_2O_2 \rightarrow 2HO^{\cdot} \quad (13)$$

$$H_2O_2 \rightarrow O_2^{2-} + 2H^+ \quad (14)$$

The improved efficiency of photodegradation in the presence of hydrogen peroxide can occur directly via conducting band electrons or indirectly via superoxide radical anions that produce hydroxyl radicals.

Photoluminescent properties

Figure 10 shows the emission spectra of $SrMoO_4$: Tb^{3+}, Sm^{3+} particles. The particles were excited at λ = 325 nm at room temperature. Figure 10a shows the broadband behavior for $SrMoO_4$ and $SrMoO_4$: 1% Sm^{3+}. Blasse and Grabmaier [63] declare that the emission of photoluminescence appears from the radiative return to the fundamental state, a phenomenon which is in agreement with the non-radiative return to the fundamental state. The energy of the excited state is used to excite the vibrations of the host lattice in the non-radiative process, i.e., heat the lattice. The radiative emission process occurs more easily if there are trapped holes or trapped electrons within the band gap. In theoretical studies referring to the photoluminescent behavior of $SrWO_4$ thin films, Orhan et al. [64] found that the existence of distorted clusters [WO_3] and [WO_4] in the $SrWO_4$ lattice would be responsible for the appearance of intermediate levels in the range of energy bands. The polarization which is favored due to the breaking of symmetry and the existence of these localized energy levels are favorable conditions for forming trapped holes and trapped electrons. The photoluminescence profiles of $SrMO_4$ and $SrMoO_4$: 1% Sm^{3+} suggest a multilevel emission mechanism, meaning a system in which relaxation occurs through several paths involving the participation of various energy states within the band interval of the material. This behavior is in agreement with other works found in the literature [65]. The $SrMoO_4$ has a maximum centered at approximately 542 nm. The effect of the matrix in the $SrMoO_4$: 1% Sm^{3+} sample is very significant, where it is possible to identify the $^4G_{5/2} \rightarrow {}^6H_{7/2}$ and $^4G_{5/2} \rightarrow {}^6H_{9/2}$ transitions at 608 and 648 nm, respectively, referring to the Sm^{3+} transitions. Photoluminescence is sensitive enough to detect the degree of structural order–disorder of the material. The degree of disorder can be addressed in different aspects as to vibrations and rotations of chemical bonds, disruptions in crystal structure, as well as the presence of structural and surface defects of particles [66].

Figure 10 **a** emission spectra of $SrMoO_4$ and of $SrMoO_4$: 1% Sm^{3+} excited by λ_{exc} = 325 nm; **b** emission spectra of $SrMoO_4$: 1% Tb^{3+}, x% Sm^{3+} (x = 1, 1.5 and 2) excited by λ_{exc} = 325 nm; **c** energy level diagram of $SrMoO_4$: 1% Tb^{3+}, x% Sm^{3+} and transfer energy processes between Tb^{3+} and Sm^{3+}.

The electronic transitions resulting from the excited state of the bandgap electrons are of type O ($2p$) → Mo ($4d$) inside the clusters $[MoO_4]^{2-}$. The electrons close to the conduction band [Mo ($4d$)] are captured by traps, which correspond to specific sites located in the bandgap, generating a recombination of the $\bar{e}$ + h pairs in the $[MoO_4]^{2-}$ clusters and subsequently emitting photons ($h\nu$) when returning to the valence band [O ($2p$)].

Many studies reported in the literature have been careful to investigate the causes and origins of

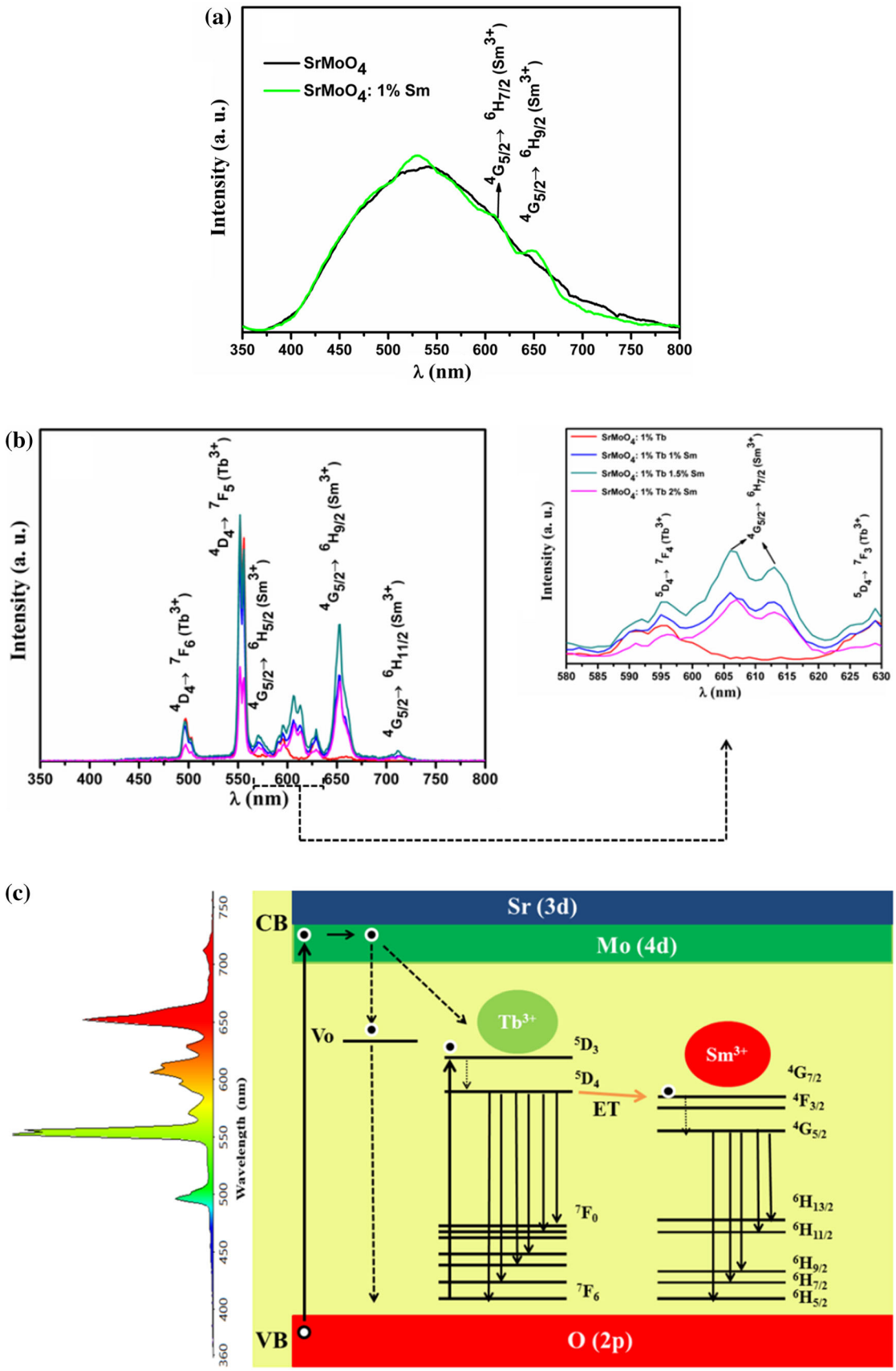
(a)
SrMoO4
SrMoO4: 1% Sm
Intensity (a. u.)
λ (nm)
4G5/2→ 6H7/2 (Sm3+)
4G5/2→ 6H9/2 (Sm3+)
(b)
Intensity (a. u.)
λ (nm)
4D4→ 7F6 (Tb3+)
4D4→ 7F5 (Tb3+)
4G5/2→ 6H5/2 (Sm3+)
4G5/2→ 6H9/2 (Sm3+)
4G5/2→ 6H11/2 (Sm3+)
SrMoO4: 1% Tb
SrMoO4: 1% Tb 1% Sm
SrMoO4: 1% Tb 1.5% Sm
SrMoO4: 1% Tb 2% Sm
5D4→ 7F4 (Tb3+)
5D4→ 7F3 (Tb3+)
(c)
Wavelength (nm)
CB
VB
Sr (3d)
Mo (4d)
O (2p)
Vo
Tb3+
Sm3+
5D3
5D4
ET
7F0
7F6
4G7/2
4F3/2
4G5/2
6H13/2
6H11/2
6H9/2
6H7/2
6H5/2

molybdate photoluminescent behavior; however, several hypotheses have been proposed to explain this behavior. According to Ding [67], the molybdate emission band is attributed to the Jahn–Teller division effect. Wu et al. [68] pointed out that the active modes of Jahn–Teller T_2 symmetry can influence the complex anion $[MoO_4]^{2-}$ with slightly distorted symmetry, which results in an electron transition absorption band of type $^1A_1 \rightarrow {}^1T_2$. Sczancoski et al. [69] consider that molybdates have the following energy states: 2*p* of oxygen located in the upper valence band and 4*d* of molybdenum located under the conduction band. Further, the type of emission is associated with the positioning of the defects in the bandgap. Blue emission is due to shallow defects (close to the valence band) related to the O-2*pσ* orbital; on the other hand, green emission is related to deep defects (slightly away from the valence band) connected to the O-2*pπ* orbital [70]. According to Lei et al. [71] regarding the complex principle $[MoO_4]^{2-}$, the coupling between the O-2*pσ* and O-2*pπ* orbitals and the Mo-4*d* (t_2) and Mo4d (e) orbitals is responsible for the hybridization of the molecular orbitals. Among these states of electrons, only the $^1A_1 \rightarrow {}^1T_2$ transition is allowed [72]. This assigns the blue emission to $^1A_1 \rightarrow {}^1T_2$ transition within $[MoO_4]^{2-}$ clusters for surface defects and orange–green emissions to defects in group MoO_3 for deep defects [73]. Other factors may influence photoluminescent properties, such as particle size, crystalline degree, morphology and surface defects [73]. Gouveia et al. [74] attribute an important role of oxygen vacancies and surface defects in the visible emission of β-Ag_2MoO_4. As in clusters $[AgO_6]$ and $[MoO_4]$, changes in morphology can be considered other important factors responsible for modifications in emission profiles of photoluminescent properties.

Figure 10b shows the PL emission spectra of the $SrMoO_4$: Tb^{3+}, Sm^{3+} particles at 325-nm excitation, showing various emission bands resulting from intra-4f transitions of the Tb^{3+} and Sm^{3+} ions orbitals. The Tb^{3+} transitions noted are: $^5D_4 \rightarrow {}^7F_J$ (J = 6, 5, 4, 3) in 495, 551 and 556, 595 and 629 nm, respectively [75]. The Sm^{3+} transitions: $^4G_{5/2} \rightarrow {}^6H_J$ (J = 5/2, 7/2, 9/2 and 11/2) are positioned at 569, 606 and 613, 652 and 712 nm obeying this order [76].

It was found that there is no presence of the band assigned to $[MoO_4]^{2-}$, as observed in $SrMoO_4$: 1% Sm^{3+}, indicating that there was a satisfactory energy transfer between $[MoO_4]^{2-} \rightarrow Tb^{3+}/Sm^{3+}$. $[MoO_4]^{2-}$ clusters have a greater ability to absorb excitation energy (*hv*), playing the role of sensitizers (**S**) and subsequently transferring part of this energy to Tb^{3+}/Sm^{3+} ions, known as activators (**A**). The energy level diagram of the $[MoO_4]^{2-}$ and Tb^{3+} and Sm^{3+} ion clusters is depicted in Fig. 10c to demonstrate the photoluminescence processes, as well as the energy transfer involved in the processes. The Tb^{3+} ions are excited by the energy transfer of the $[MoO_4]^{2-}$ clusters. The excited states of Tb^{3+} ($^5D_3$ and $^5D_4$) are occupied. The electrons of the $^5D_3$ level relax to the $^5D_4$ level due to the non-radiation by relaxation processes. The specific emissions of Tb^{3+} denominated $^5D_4 \rightarrow {}^7F_J$ (J = 0–6) that occur between 488 and 628 nm are verified. Part of the energy of Tb^{3+} ($^5D_4$) is transferred to the $^4F_{3/2}$ level of Sm^{3+}. The non-radioactive relaxation $^4F_{3/2} \rightarrow {}^4G_{5/2}$ of Sm^{3+} is identified in the level diagram. After the $^4G_{5/2}$ level is occupied, Sm^{3+} $^4G_{5/2} \rightarrow {}^6H_J$ emissions (J = 13/2, 11/2, 9/2, 7/2, 5/2) are observed between 563 and 712 nm. The Tb^{3+} emission bands generally have a good overlap with some Sm^{3+} excitation bands, and consequently, efficient energy transfer between Tb^{3+} and Sm^{3+} has been successfully demonstrated in several host matrices such as: $CaLa_2(MoO_4)_4$: Tb^{3+}/Sm^{3+}, $Ba_3La(PO_4)_3$: Tb^{3+}/Sm^{3+}, $KBaY(MoO_4)_3$: Tb^{3+}, Eu^{3+}, Sm^{3+} and Tb^{3+}/Eu^{3+} [77–79].

The most common valence state of rare-earth ions is the trivalent one. Some ions are inclined to exist in abnormal valency, such as Sm^{2+}, Eu^{2+}, Yb^{2+} and Ce^{4+}, Pr^{4+}, Tb^{4+}, because they all have a stable electronic configuration ($4f_0$, $4f_7$ or $4f_{14}$). When a pair of conjugate electronic configuration rare-earth ions co-doped in one matrix, they tend to transfer an electron in order to get a more stable configuration under suitable condition.

Chen et al. [80] attributes that photostimulated factors of luminescence of rare-earth ions can occur in phosphors that contain RE^{4+} type ions and some trapped electrons (in color centers). The electrons released from the color centers can recombine with the RE^{4+} ions to provide a photo-stimulated luminescence of the RE^{3+} ion. The Tb^{4+} ion can be transformed into Tb^{3+} from the release of an electron, according to the expression (15):

$$Tb^{4+} + e^- \rightarrow Tb^{3+} + hv \quad (15)$$

Although no Tb^{4+} transition was observed in the photoluminescence emission spectra, the existence of

Tb^{4+} ions can be considered, paying attention to the investigation carried out by Nugent [81]. According to his investigation, the appearance of RE^{4+} ions is possible if the optical electronegativity $(\chi(RE^{4+}))$ is less than or equal to 3.03, and the standard reduction potential $E^0_{RE}(RE^{4+} \rightarrow RE^{3+})$ is less than or equal to 5.2 V. The $\chi(Tb^{4+})$ is 2.55 and the $E^0_{RE}(Tb^{4+} \rightarrow Tb^{3+})$ is 3.30 V [81], favoring the appearance of Tb^{4+} ions.

The Tb^{4+} ion in the $SrMoO_4$ lattice must replace two Sr^{2+} ions and generate a Sr^{2+} vacancy as a mechanism to neutralize the charges in the matrix. The electrons released from Tb^{4+} ions are responsible for the appearance of Tb^{3+} ions. Level $^5D_3$ is populated and decay non-radioactively to level $^5D_4$. The electronic transitions of Tb^{4+} $^5D_4 \rightarrow {}^7F_J$ (J = 0–6) are clearly shown between 488 and 628 nm.

The performance of rare-earth ion-activated photoluminescent materials can be considerably affected by the concentration of these doping ions [82]. It is observed that there is a decrease in photoluminescence intensity for concentrations higher than the $SrMoO_4$: 1% Tb^{3+}, 1% Sm^{3+} sample. This behavior, known in the literature as quenching concentration, is promoted by decreasing the distance between activating ions. Then, it is possible to obtain the critical distance (CD) from the quenching concentration at which the non-radioactive rate equals the internal relaxation of the ion. The concentration quenching might be due to non-radiative energy transfer from one activator ion to another activator ion. Non-radiative energy transfer takes place via two different mechanisms, i.e., (1) Förster resonance energy transfer (multipole–multipole interaction) and (2) dexter mechanism (exchange interaction).

At Förster resonance energy transfer (FRET), energy transfer occurs when the activator (or sensitizer) is in the excited state. FRET is based on the classic dipole–dipole interactions between activator and activator dipole transitions and is significantly dependent on the distance between (A) and (A), falling at a rate of $1/R^6$. FRET can typically occur at distances up to 100 Å [83]. Dexter energy transfer is a short-range phenomenon (CD = 10 Å) that decreases with e^{-R} and depends on the spatial overlap of sensitizing and inhibiting molecular orbitals. For the quenching concentration, Blasse [84] assumed that the shortest average distance between the closest activating ions is equal to the critical distance (CD). The CD value can be practically calculated using Eq. (16):

$$CD = 2x\left(\frac{3V}{4\pi X_c N}\right)^{1/3} \tag{16}$$

where Xc is the quenching concentration, N is the number of units of the molecular formula per unit cell, and V is the unit cell volume. Values of V and N for the crystalline $SrMoO_4$ (tetragonal system, one cell unit of $SrMoO_4$ comprising of 4 formula units) are 351.02 $Å^3$ and 4, respectively (JCPDS No Card 850586). Considering X_c = 2.5% (0.025), critical distance CD in $SrMoO_4$: 1% Tb^{3+}, 1.5% Sm^{3+} particles was calculated to be 20.31 Å. In this case, the rare-earth ions distance is larger than 10 Å. Thus, the exchange interactions are ruled out. Therefore, electric multipolar interaction is believed to be the only mode for energy transfer among the rare-earth ions in $SrMoO_4$ particles.

The chromaticity coordinates were calculated from the emission spectrum distribution, as shown in Fig. 11, with their respective light images emitted for each sample. Blank emission was obtained for $SrMoO_4$ (0.33, 0.40) and $SrMoO_4$: 1% Sm^{3+} (0.31, 0.40)

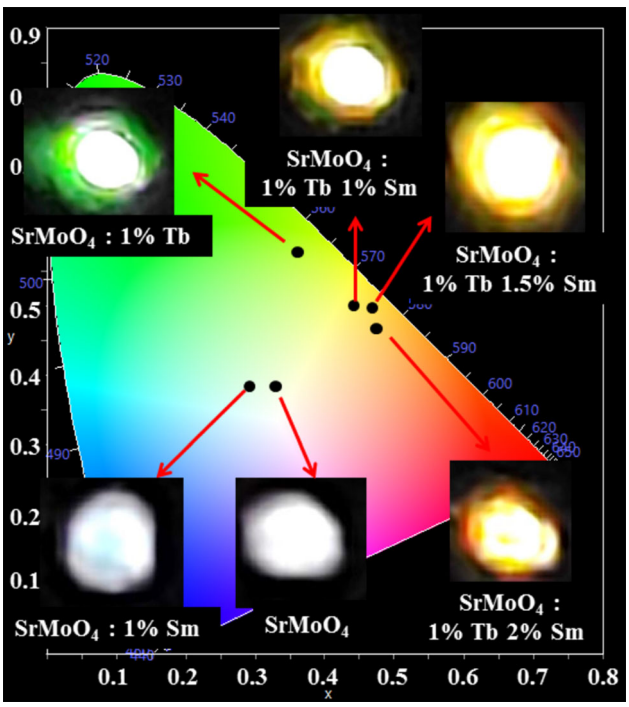

Figure 11 Chromaticity diagram with the induction of CIE coordinates and photos of the light emitted by each sample.

due to simultaneous emissions in the blue, green and red regions, as shown in Fig. 11a. Fair cooperation of emissions in the visible regions made it possible to generate white light. Other light properties such as color reproducibility index (CRI), color temperature (CCT) and purity (%) were evaluated and are reported in Table S4 of the supplementary information.

As the Sm^{3+} concentration increases, the color temperature decreases, thus tending to warmer colors as depicted in the chromaticity diagram. Co-doped $SrMoO_4$ samples obtained greater than 80% color purity, indicating little combination with other regions.

The luminous efficacy (LE) values of the emission spectra were calculated to evaluate the emission brightness of $SrMoO_4$ and of $SrMoO_4$: 1% Sm^{3+} for the human eye. These values were based on Eq. (17) [85]:

$$\mathrm{LE} = 683x\frac{\int I(\lambda)V(\lambda)d(\lambda)}{\int I(\lambda)d(\lambda)} \tag{17}$$

Here, $I(\lambda)$ is emission spectrum of the sample and $V(\lambda)$ is the human eye sensitivity curve. The human eye is the most sensitive to the 555 nm electromagnetic radiation; therefore, the highest possible luminous efficacy value of 683 lm/W_{opt} is obtained for monochromatic green light at 555 nm. The LE values obtained for the $SrMoO_4$ and $SrMoO_4$: 1% Sm^{3+} samples were 310 and 315 lm/W_{opt}, respectively. The results presented by LE demonstrate a large amount of lumens per generated power, which means an efficient light source with less electrical costs. The high LE and CRI values indicate that the synthesized material has fundamental properties for applicability in WLEDs.

The first WLED occurred by producing a combination of a blue LED chip and YAG:Ce^{3+} yellow-emitting phosphor, which is the conventional method in lighting and display areas. However, YAG:Ce^{3+} yellow phosphors suffer some deficiencies, due to the deficiency of the red emission component resulting in low CRI and low LE, which limits its applicability to some extent. To overcome this challenge, some red phosphors are added to the light source. However, often used red nitride phosphors are very expensive and require synthesis techniques, which restricts their use. To optimize the color rendering properties of white and colored light phosphors, the focus of their fabrication shifts gradually from the YAG:Ce^{3+}-based to the red–green–blue (RGB)-emitting color phosphors excited by ultraviolet-LEDs. However, the main deficiency of these WLEDs is their low luminescence efficiency due to the strong absorption of blue emission by red and green phosphors [86]. Multicolored phosphors have a certain complexity in their production because they are prepared individually, the particle size of the individual the phosphorus must be adapted to each other to avoid agglomeration or sedimentation, and the final product must be mixed homogeneously in exact proportions [87]. Single-phase phosphors have great advantages when compared to multicolored phosphors, as they have greater luminescent efficiency, lower manufacturing costs, easier manufacturing processes, higher color rendering index and better reproducibility [88]. UV LEDs coated with single-phase phosphors are promising candidates for the production of WLEDs.

Comparing the $SrMoO_4$ and $SrMoO_4$: 1% Sm^{3+} samples with other systems such as: $(Ba,Sr)_2SiO_4$:Eu^{2+}/$CaAlSiN_3$:Eu^{2+} (LE = 51 lm/W_{opt}) [89], K_2SiF_6:Mn^{4+} (LE = 14–173 lm/W_{opt}) [90] and $Eu_2Mo_4O_{15}$ (LE = 208 lm/W_{opt}) [91], we observed that the LE presented by the materials produced by this work showed higher values and the CRI values showed approximate values. However, the photometric parameters duly meet the criteria for an excellent phosphor for use in WLEDs.

Therefore, rare-earth activated molybdate phosphors with outstanding chemical stability and high luminous efficiency are much needed for the development of solid-state lighting devices. The molybdates activated with rare-earth ions have been gaining increasing attention owing to their strong visible-light emission under UV illumination. By doping molybdates with different rare-earth ions, several emissive colors ranging from the ultraviolet (UV) to infrared (IR) regions can be achieved owing to the existing transitions within the 4f-4f and 5d-4f configurations of the rare-earth ions [92].

Conclusion

In summary, the $SrMoO_4$: Tb^{3+}, Sm^{3+} series showed tunable colors from white ($SrMoO_4$, $SrMoO_4$: 1% Sm^{3+}), to green ($SrMoO_4$: 1% Tb^{3+}), to orange ($SrMoO_4$: 1% Tb^{3+}, x% Sm^{3+}, x = 1, 1.5 and 2%) due to the effect of the dopant type and concentration.

After excitation at 325 nm, the material shows the intense green emissions of Tb^{3+} [$^5D_4 \rightarrow {}^7F_J$ (J = 6, 5, 4, 3] and the characteristic emissions of Sm^{3+} in red–orange [$^4G_{5/2} \rightarrow {}^6H_J$ (J = 5/2, 7/2, 9/2 and 11/2)]. The effect of the quenching concentration at X_{c-} = 0.025 on photoluminescence suppression due to multipolar interactions between activating ions was evaluated. The energy transfer was observed between Tb^{3+} ($^5D_4$) and Sm^{3+} ($^4G_{5/2}$). The particle growth stages were proposed from the nucleation stages and subsequent growth stages from self-assembly processes. Different morphologies were observed, which correspond to intermediate stages of particle growth. The photocatalytic activities were evaluated, showing the best performance of the $SrMoO_4$ and $SrMoO_4$: 1% Sm^{3+} samples with 100% efficiency in methyl orange degradation in 45 min with the aid of H_2O_2.

Acknowledgements

The authors thank the following Brazilian research financing institutions for financial support: the National Council for Scientific and Technological Development (*CNPq*), the Coordination for the Improvement of Higher Education Personnel (*CAPES*), Brazil, and the Graduate Program in Materials Science and Engineering (*PPGCEM/UFRN*).

Compliance with ethical standards

Conflict of interest The authors declare that they have no known competing financial interests or personal relationships that could have appeared to influence the work reported in this paper.

Electronic supplementary material: The online version of this article (https://doi.org/10.1007/s10853-020-04623-5) contains supplementary material, which is available to authorized users.

References

[1] Santiago AAG, Lovisa LX, Medeiros PN et al (2019) Fast and simultaneous doping of $Sr_{0.9-x-y-z}Ca_{0.1}In_2O_4$:($xEu^{3+}$, yTm^{3+}, zTb^{3+}) superstructure by ultrasonic spray pyrolysis. Ultrason Sonochem 56:14–24

[2] Lovisa LX, Santiago AAG, Farias MB et al (2018) White light emission from single-phase Y2MoO6: xPr^{3+} (x = 1, 2, 3 and 4 mol%) phosphor. J Alloys Compd 769:420–429

[3] Voronko YK, Sobo AA (1976) Exchange mechanism of nonradiative energy transfer between rare-earth ions in crystals. SOy Phys JETP 42:525

[4] Uitert LGV (1971) Energy transfer between rare earth ions in tungstates. J Lumin 4:1

[5] Lovisa LX, Fernandes YLRL, Garcia LMP et al (2019) Tb^{3+}/Pr^{3+} co-doped $ZnMoO_4$ phosphor with tunable photoluminescence and energy transfer processes. Opt Mater 96:109332

[6] Tranquilin R, Lovisa LX, Almeida C et al (2019) Understanding the white-emitting $CaMoO_4$ Co-doped Eu^{3+}, Tb^{3+}, and Tm^{3+} phosphor through experiment and computation. J Phys Chem C 123:18536–18550

[7] Pavani K, Kumar JS, Moorthy LR (2014) Luminescence properties of single-phase $SrMg_2La_2W_2O_{12}$:Tb^{3+}, Sm^{3+}, Tm^{3+} phosphor for multicolor- and white light-emitting. Mater Res Express 1:016201

[8] Park SW, Moon BK, Jeong JH, Bae JS, Kim JH (2015) Crystal structure, electronic structure, and photoluminescent properties of $SrMoO_4$:Tb^{3+} phosphors. Mater Res Bull 70:403–411

[9] Guan L et al (2011) Synthesis and optical properties of Dy^{3+}, Li^+ doped $CaMoO_4$ phosphor. J Rare Earths 29:540–543

[10] Gan CL, Xu XL, Yang JH, Peng ZF (2015) Preparation and luminescence properties of $SrMoO_4$ doped with Pr^{3+}. Key Eng Mater 633:253–256

[11] Gurgel GM, Lovisa LX, Pereira LM et al (2017) Photoluminescence properties of (Eu, Tb, Tm) co-doped $PbMoO_4$ obtained by sonochemical synthesis. J Alloys Compd 700:130–137

[12] Van Loef EVD et al (2001) High-energy-resolution scintillator: Ce^{3+} activated LaBr 3. Appl Phys Lett 79:1573–1575

[13] Justel T, Nikol H (2000) Optimization of luminescent materials for plasma display panels. Adv Mater 12:527–530

[14] Bi J, Wu L, Zhang Y, Li Z, Li D, Fu X (2009) Solvothermal preparation, electronic structure and photocatalytic properties of $PbMoO_4$ and $SrMoO_4$. Appl Catal B Environ 91:135–143

[15] Li G, Lan S, Li L, Li M, Bao W, Zou H, Xu X, Gan S (2012) Tunable luminescence properties of NaLa(MoO4)2:Ce^{3+}, Tb^{3+} phosphors for near UV-excited white light-emitting-diodes. J Alloys Compd 513:145–149

[16] Choi GK, Cho SY, An JS, Hong KS (2006) Microwave dielectric properties and sintering behaviors of scheelite compound $CaMoO_4$. J Eur Ceram Soc 26:2011–2015

[17] Shivakumara C, Saraf R (2015) Eu^{3+}-activated $SrMoO_4$ phosphors for white LEDs applications: synthesis and structural characterization. Opt Mater 42:178–186

[18] Xu L et al (2007) Synthesis and properties of Eu^{3+} activated strontium molybdate phosphor. J Rare Earths 25:706–709
[19] Yang P, Li C, Wang W, Quan Z, Gai S, Lin G (2009) Uniform $AMoO_4$: Ln (A = Sr^{2+}, Ba^{2+}; Ln = Eu^{3+}, Tb^{3+}) submicron particles: solvothermal synthesis and luminescent properties. J Solid State Chem 182:2510–2520
[20] Niu N, Yang P, Wang W, Fei H, Gai S, Wang D, Lin J (2011) Solvothermal synthesis of $SrMoO_4$: Ln (Ln = Eu^{3+}, Tb^{3+}, Dy^{3+}) nanoparticles and its photoluminescence properties at room temperature. Mater Res Bull 46:333–339
[21] Almeida CRR, Lovisa LX, Santiago AAG et al (2017) One-step synthesis of $CaMoO_4$: Eu^{3+} nanospheres by ultrasonic spray pyrolysis. J Mater Sci Mater Electron 28:16867–16879
[22] Abakumov AM, Morozov VA, Tsirlin AA, Verbeeck J, Hadermann J (2014) Cation ordering and flexibility of the $(BO4)_2$—tetrahedra in incommensurately modulated $CaEu_2(BO4)_4$ (B = Mo, W) cheelites. Inorg Chem 53:9407–9415
[23] Shannon R (1976) Revised effective ionic radii and systematic studies of interatomic distances in halides and chalcogenides. Acta Crystallogr Sect A 32:751–767
[24] Zhang ZW, Shen XH, Ren YJ, Hou WL, Zhang WG, Wang DJ (2014) Influence of Al^{3+} ions on the enhancement of the fluorescence in the $CaMoO_4$:Sm^{3+} phosphor. Opt Laser Technol 56:348–353
[25] Chen D, Tang K, Li F, Zheng H (2006) A simple aqueous mineralization process to synthesize tetragonal molybdate microcrystallites. Cryst Growth Des 6:247–252
[26] Ouyang G, Yang G, Sun C, Zhu W (2008) Nanoporous structures: smaller is stronger. Small 4:1359–1362
[27] Zhu Z, Zhang A, Ouyang G, Yang G (2011) Band gap tunability in semiconductor nanocrystals by strain: size and temperature effect. J Phys Chem C 115:6462–6466
[28] Toby B (2001) EXPGUI, a graphical user interface for GSAS. J Appl Crystallogr 34:210–213
[29] McKelvy MJ et al (2001) Magnesium hydroxide dehydroxylation: in situ nanoscale observations of lamellar nucleation and growth. Chem Mater 13:921–926
[30] Motta FV, Marques APA, Li MS et al (2013) Preparation and photoluminescence characteristics of $In(OH)_3$:$x$$Tb^{3+}$ obtained by microwave-assisted hydrothermal method. J Alloys Compd 553:338–342
[31] Sczancoski JC, Cavalcante LS, Joya MR, Espinosa JWM, Pizani PS, Varela JA, Longo E (2009) Synthesis, growth process and photoluminescence properties of $SrWO_4$ powders. J Colloid Interface Sci 330:227–236
[32] Sczancoski JC, Cavalcante LS, Joya MR, Varela JA, Pizani PS, Longo (2008) $SrMoO_4$ powders processed in microwave-hydrothermal: synthesis, characterization and optical properties. Chem Eng J 140:632–637
[33] Thongtema T, Kungwankunakorn S, Kuntalue B, Phuruangrat A, Thongtem A (2010) Luminescence and absorbance of highly crystalline $CaMoO_4$, $SrMoO_4$, $CaWO_4$ and $SrWO_4$ nanoparticles synthesized by co-precipitation method at room temperature. J Alloys Compd 506:475–481
[34] Manjón FJ, Garro N, Pellicer-Porres J et al (2006) Lattice dynamics study of scheelite tungstates under high pressure $BaWO_4$. Phys Rev B 74:144111
[35] Porto SPS, Scott JF (1967) Raman spectra of $CaWO_4$, $SrWO_4$, $CaMoO_4$ and $SrMoO_4$. Phys Rev 157:716–719
[36] Thongtem T, Phuruangrant A, Thongtem S (2008) Characterization of MEWO4 (ME = Ba, Sr and Ca) nanocrystallines prepared by sonochemical method. Appl Surf Sci 254:7581–7585
[37] Cavalcante LS et al (2009) Photoluminescent behavior of $BaWO_4$ powders processed in microwave-hydrothermal. J Alloys Compd 474:195–200
[38] Ling ZCX, Xia HR, Ran DG et al (2006) Lattice vibration spectra and thermal properties of $SrWO_4$ single crystal. Chem Phys Lett 426:85–90
[39] Gong Q, Qian X, Ma X, Zhu Z (2006) Large-scale fabrication of novel hierarchical 3D $CaMoO_4$ and $SrMoO_4$ mesocrystals via a microemulsion-mediated route. Cryst Growth Des 6:1821–1825
[40] Cavalcante LS, Sczancoski JC, Batista NC, Longo E, Varela JA, Orlandi MO (2013) Growth mechanism and photocatalytic properties of $SrWO_4$ microcrystals synthesized by injection of ions into a hot solution aqueous. Adv Powder Technol 24:344–353
[41] Mao JG, Geng J, Wu XC, Zhu JJ (2010) Selective synthesis and luminescence properties of self-assembled $SrMoO_4$ superstructures via a facile sonochemical route. J Phys Chem C 114:1982–1988
[42] Jiang W, Zhu W, Peng C, Yang F, Xuan S, Gong X (2012) Controllable synthesis of hierarchical strontium molybdate by sonochemical method. Cryst Res Technol 47:997–1003
[43] Li WH, Zhang XZ (2010) A study of the magnetorheological effect of bimodal particle based magnetorheological elastomers. Smart Mater Struct 19:035002
[44] Banfield JF, Welch SA, Zhang H, Ebert TT, Penn RL (2000) Aggregation-based crystal growth and microstructure development in natural iron oxyhydroxide biomineralization products. Science 289:751–754
[45] Banfield RL, Banfield JF (1998) Imperfect oriented attachment: dislocation generation in defect-free nanocrystals. Science 281:969–971
[46] Pires AM, Santos MF, Davolos MR, Stucchi EB (2002) The effect of Eu^{3+} ion doping concentration in Gd_2O_3 fine spherical particles. J Alloys Compd 344:276–279

[47] Zhao X, Tan MC (2015) Ce dopant effects on $NaYF_4$ particle morphology and optical properties. J Mater Chem C 3:10207
[48] Mary CM, Vimal G et al (2016) Growth and characterization of Sm^{3+} doped cerium oxalate single crystals. J Mater Res Technol 5:268–274
[49] Suzuki K, Kijima K (2005) Optical band gap of barium titanate nanoparticles prepared by RF-plasma chemical vapor deposition. J Appl Phys 44:2081–2082
[50] Park CH, Keszler DA, Yanagi H, Tate J (2003) Gap modulation in MCu[Q1 − $xQ'x$]F (M = Ba, Sr; Q, Q′ = S, Se, Te) and related materials. Thin Solid Films 445:288–293
[51] Wood DL, Tauc J (1972) Weak absorption tails in amorphous semiconductors. Phys Rev B Condens Matter 5:3144
[52] Marques APA, Leite ER, Varela JA, Longo E (2008) Effect of variations in annealing temperature and metallic cations on nanostructured molybdate thin films. Nanoscale Res Lett 3:152–157
[53] Longo VM et al (2008) Structural conditions that leads to photoluminescence emission in $SrTiO_3$: an experimental and theoretical approach. J Appl Phys 104:023515
[54] Longo E et al (2014) Toward an understanding of the growth of Ag filaments on α-Ag_2WO_4 and their photoluminescent properties: a combined experimental and theoretical study. J Phys Chem C 118:1229–1239
[55] Zhu YN, Zheng GH, Dai ZX, Mu JJ, Yao ZF (2017) Monodisperse $SrMoO_4$ nanocrystals: synthesis, luminescence andphotocatalysis. J Mater Sci Technol 33:834–842
[56] Sczancoski JC et al (2009) Morphology and blue photoluminescence emission of $PbMoO_4$ processed in conventional hydrotherma. J Phys Chem C 113:5812–5822
[57] Paradelas SM, Gonçalves RF, Motta FV, Lima RC, Li MS, Longo E, Marques APDA (2017) Effects of microwave-assisted hydrothermal treatment and of use of capping reagent on the photophysical properties of $SrMoO_4$ phosphors. J Lumin 192:818–826
[58] Pradeep T (2007) Understanding nanoscience and nanotechnology. McGraw-Hill, New York
[59] Gracia L, Longo VM, Cavalcante LS, Beltran A, Avansi W, Li MS, Mastelaro VS, Varela JA, Longo E, Andre J (2011) Presence of excited electronic state in $CaWO_4$ crystals provoked by a tetrahedral distortion: an experimental and theoretical investigation. J Appl Phys 110:043501–043511
[60] Kusuma M, Jagannath KV (2019) Solution combustion synthesis of $SrMoO_4$ nanophosphor using different molybdenum sources and study of its photocatalytic properties. Mater Res Express 6:1050a
[61] Hosseinpour-mashkani SM, Sobhani-nasab A, Mehrzad M (2016) Controlling the synthesis $SrMoO_4$ nanostructures and investigation its photocatalyst application. J Mater Sci Mater Electron 27:5758–5763
[62] Nezar S, Laoufi N (2018) Electron acceptors effect on photocatalytic degradation of metformin under sunlight irradiation. Sol Energy 164:267–275
[63] Blasse G, Grabmaier BC (1994) Luminescent materials. Springer, Berlin
[64] Orhan E et al (2005) Conditions giving rise to intense visible room temperature photoluminescence in $SrWO_4$ thin films: the role of disorder. Chem Phys 312:1
[65] Longo VM, Cavalcante LS, De Figueiredo AT, Santos LPS, Longo E, Varela JA, Sambrano JR, Paskocimas CA, De Vicente FS, Hernandes AC (2007) Highly intense violet-blue light emission at room temperature in structurally disordered $SrZrO_3$ powders. Appl Phys Lett 90:091906
[66] Santiago AAG et al (2018) Photoluminescent properties of the $Ba_{1-x}Zn_xMoO_4$ heterostructure obtained by ultrasonic spray pyrolysis. Ceram Int 44:3775–3786
[67] Ding SS et al (2013) Morphology evolution and photoluminescence of barium molybdate controlled by poly (sodium-4-styrenesulfonate). J Alloys Compd 579:549–552
[68] Wu XY et al (2007) Aqueous mineralization process to synthesize uniform shuttle-like $BaMoO_4$ microcrystals at room temperature. J Solid State Chem 180:3288–3295
[69] Sczancoski JC et al (2010) Electronic structure and optical properties of $BaMoO_4$ powders. Curr Appl Phys 10:614–624
[70] Longo VM, Cavalcante LS, Erlo R, Mastelaro VR, De Figueiredo AT, Sambrano JR, De Lazaro S, Freitas AZ, Gomes L, Vieira ND Jr, Varela JA, Longo E (2008) Strong violet–blue light photoluminescence emission at room temperature in $SrZrO_3$: joint experimental and theoretical study. Acta Mater 56:2191
[71] Lei M et al (2015) Controllable route to barium molybdate crystal and their photoluminescence. J Alloys Compd 639:102–105
[72] Yin Y et al (2013) One-step fabrication of $BaMoO_4$ microstructures with controlled morphologies via a simple EDTA-mediated route. Superlattices Microstruct 55:109–117
[73] Xie A, Yuan X, Hai S, Wang J, Wang F, Li L (2009) Enhancement emission intensity of $CaMoO_4$: Eu^{3+}, Na^+ phosphor via Bi co-doping and Si substitution for application to white LEDs. J Phys D Appl Phys 42:105107
[74] Gouveia AF et al (2014) Experimental and theoretical investigations of electronic structure and photoluminescence properties of β-$Ag2MoO_4$ microcrystals. Inorg Chem 53:5589–5599
[75] Lin X, Qião X, Fan X (2011) Synthesis and luminescence properties of a novel red $SrMoO_4$: Sm^{3+}, R^{3+} phosphor. Solid State Sci 13:579–583
[76] Singh NP, Singh NR, Singh NM (2018) Synthesis of $CdMoO_4$:Sm^{3+} phosphors at room temperature and investigation on photoluminescence. Optik 158:365–373

[77] Xie W, Liu G, Dong X, Wang J, Wensheng J (2015) A direct warm-white-light $CaLa_2(MoO_4)_4$: Tb^{3+}, Sm^{3+} phosphor with tunable color tone via energy transfer for white LEDs. RSC Adv 5:77866–77872

[78] Zhou W, Gu M, Ou Y, Zhang C, Zhang X, Zhou L, Liang H (2017) Concentration-driven selectivity of energy transfer channels and color tunability in $Ba_3La(PO_4)_3$:Tb^{3+}, Sm^{3+} for warm white LEDs. Inorg Chem 56:7433–7442

[79] Li K, Van Deun R (2018) Photoluminescence and energy transfer properties of a novel molybdate $KBaY(MoO_4)3$:-Ln^{3+} (Ln^{3+} = Tb^{3+}, Eu^{3+}, Sm^{3+}, Tb^{3+}/Eu^{3+}, Tb^{3+}/Sm^{3+}) as a multi-color emitting phosphor for UV w-LEDs. Dalton Trans 47:6995–7004

[80] Chen W, Sammynaiken R, Huang Y (2000) Photoluminescence and photostimulated luminescence of Tb^{3+} and Eu^{3+} in zeolite-Y. J Appl Phys 88:1424–1431

[81] Nugent LJ (1975) Standard electrode potentials and enthalpies of formation of some lanthanide and actinide aquo-ions. J Inorg Nucl Chem 37:1767–1770

[82] Yu J, Huang K, Yuan L, Feng S (2014) Hydrothermal syntheses and photoluminescence properties of rare-earth tungstate as near ultraviolet type red phosphors. New J Chem 38:1441–1445

[83] Jena P, Grupta SK, Natarajan V, Sahu M, Satyanarayana N, Venkateswarlu M (2015) Structural characterization and photoluminescence properties of sol–gel derived nanocrystalline $BaMoO_4$:Dy^{3+}. J Lumin 158:203–210

[84] Blasse G (1986) Energy transfer between inequivalent Eu^{2+} ions. J Solid State Chem 62:207

[85] Smet PFP, Poelman D (2011) Selecting conversion phosphors for white light-emitting diodes. J Electrochem Soc 158:R37–R54

[86] Guo Bin, Zhang Zhi-Wei, Jiang Da-Guo, Li Yu-Nong, Sun Xin-Yuan (2019) Generation of bright white-light by energy-transfer strategy in $Ca_{19}Zn_2(PO_4)_{14}$:Ce^{3+}, Tb^{3+}, Mn^{2+} phosphors. J Lumin 206:244–249

[87] Panigrahi K, Saha S, Sain S, Chatterjee R, Das A, Ghorai UK, Sankar Das N, Chattopadhyay KK (2018) White light emitting $MgAl_2O_4$:Dy^{3+}, Eu^{3+} nanophosphor for multi-functional applications. Dalton Trans 47:12228–12242

[88] Lü W, Xu H, Huo J, Shao B, Feng Y, Zhao S, You H (2017) Tunable white light of a Ce^{3+}, Tb^{3+}, Mn^{2+} triply doped Na2Ca3Si2O8 phosphor for high colour-rendering white LED applications: tunable luminescence and energy transfer. Dalton Trans 46:9272–9279

[89] Won YH, Jang HS, Chon KW, Song YS, Jeon DY, Kwon HK (2009) Effect of phosphor geometry on the luminous efficiency of high-power white light-emitting diodes with excellent color rendering property. Opt Lett 34:1–3

[90] Oh JH, Kang H, Eo YJ, Park HK, Do YR (2011) Synthesis of narrow-band red-emitting K_2SiF_6:Mn^{4+} phosphors for a deep red monochromatic LED and ultrahigh color quality warm-white LEDs. J Mater Chem C 3:607

[91] Janulevicius M, Grigorjevaite J, Merkininkaite G, Sakirzanovas S, Katelnikovas A (2016) Luminescence and luminescence quenching of $Eu_2Mo_4O_{15}$. J Lumin 179:35–39

[92] Wang Z, Liang H, Zhou L, Wang J, Gong M, Su Q (2008) $NaEu_{0.96}SM_{0.04}(MoO_4)_2$ as a promising red-emitting phosphor for LED solid-state lighting prepared by the Pechini process. J Lumin 128:147–154